Chapter: III

Investigation of the Origin for Suppression of Charge Ordering Transition in Nanocrystalline $Ln_{0.5}Ca_{0.5}MnO_3$ (Ln = La, Nd, Pr) Ceramics

Chapter-III

3.1 Introduction

As discussed in section 1.9 of chapter I, it is reported recently in several doped rare earth perovskite manganites that when the particle size is reduced to nanoscale, the low temperature charge and orbitally ordered insulating state is destabilized, with suppression of charge ordering transition and stabilization of high temperature ferromagnetic metallic state down to low temperatures. However, there is no unanimity on the origin of suppression of this charge ordering transition in half doped rare earth perovskite manganites and different authors have made different propositions like core-shell structure, effective excess pressure due to small size of the samples etc. The reason for suppression of charge ordering transition in nanocrystalline form is reported variously by different authors [Giri et al. (2011); Sarkar et al. (2007); Lu et al. (2007)]. In LCMO and PCMO it is reported that charge ordering transition is suppressed due to the enhanced surface disorder in the nano size samples [Giri et al. (2011); Sarkar et al. (2007)]. Similarly in NCMO it is reported that antiferromagnetic phases disappear in the nanoparticles making way for an emergence of ferromagnetic metallic phase [Pramanik et al. (2010)]. The actual reason of the absence of charge ordering transition in nanocrystalline form of these manganites and origin of FM state is still a controversial issue and matter of great debate.

Further, there are contradictory reports about the effects of particle size reduction on the unit cell volume of the manganites. Since the unit cell volume and orthorhombic strain [Zhang et al. (2009)] have great impact on the magnetic state of the doped rare earth perovskite manganites there is a need to unambiguously ascertain the effect of particle size on the unit cell volume. There are some papers which report the lowering of unit cell volume with decreasing particle size in $La_{0.5}Ca_{0.5}MnO_3$ [Pramanik et al. (2010); Das et al. (2011)], $Pr_{0.5}Ca_{0.5}MnO_3$ [Das et al. (2011); Auslender et al. (2010)], while several authors have reported the enhancement of the unit cell volume with decreasing particle size [Jirak et al. (2010); Auslender et al. (2010); Rozenberg et al. (2009)]. Many authors have reported that there is no significant change in the unit cell volume by changing the particle size in nanocrystalline manganites [Rao et al. (2005); Jirak et al. (2010)]. Thus the effect of particle size reduction on the unit cell volume of nanocrystalline manganites needs to be settled to arrive at the actual reason of suppression of charge ordering transition. Recently using density functional theory (DFT) and dynamical mean field theory (DMFT) calculations on LCMO, Das et al. (2011) have reported that destabilization of low temperature antiferromagnetic phase in nanocrystalline samples is related to the structural changes in the samples. Das et al. (2011) have validated the work of Sarkar et al. (2008) who have reported the reduction of unit cell volume with decreasing particle size. The results of Das et al. (2011) and Sarkar et al. (2008) have been challenged by Markovich et al. (2012), who referred to the work of several other groups [Jirak et al. (2010); Auslender et al. (2010); Rozenberg et al. (2009)], where enhancement of unit cell volume with decreasing particle size is observed. In order to find out a decisive answer for the effect of particle size variation on the unit cell volume of nanocrystalline manganites, and origin of suppression of charge ordering transition, we have investigated three series of the $Ln_{0.5}Ca_{0.5}MnO_3$ (Ln=La, Nd, Pr) samples. We find that the nanocrystalline samples of all the three manganite systems show significant enhancement of the unit cell volume with decreasing particle size. The associated orthorhombic strain and coordinates of the atoms in the unit cell are also modified significantly with this structural change, caused by the reduction of the particle size. The increased unit cell volume is attributed to enhancement of the e_g -electron bandwidth thereby stabilizing the ferromagnetic state down to low temperatures in nanocrystalline samples.

3.2 Experimental Details

The samples were synthesized by combustion method. Details of sample synthesis are given in chapter II. The powder from same precursor was calcined to various temperatures to get the samples of various crystallite sizes. The samples calcined at 600, 700, 800, 900, 1000, 1100, 1200, 1300 and 1400 ^{o}C are denoted as C6, C7, C8, C9, C10, C11, C12, C13 and C14 respectively. The XRD data were analyzed by Rietveld structure refinement using FULLPROF suite [Carvajal 2011]. In the refinements, pseudo-Voigt function was used to model the background while sixth coefficient polynomial was used to model the profile shape. We have used the micro structural strain parameters during refinement of the structure to model the anisotropic peak broadening in the diffraction profiles. The particle size of the nanocrystalline samples were calculated by Rietveld method for which the XRD profiles were modeled by the function given by Thompson Cox and Hasting [Carvajal 2011].

3.3 Results and Discussion

3.3.1 Microstructural and Spectroscopic Analysis of the Samples

The microstructure, composition and Mn^{4+}/Mn^{3+} ratio of the samples were analysed by SEM, TEM, EDS and XPS measurements. Figs. 3.1(a, b) show the SEM micrographs of the nanocrystalline (calcined at 800 ^{o}C) and bulk (calcined at 1400 ^{o}C) LCMO samples. The bulk sample exhibits clearly resolved grains of submicron sizes while some of the grains are anomalously grown to more than 1 µm. The nano sample does not show the clearly resolved grains as the most of the grain boundaries are fused together in combustion synthesis. The size of the resolved grains is estimated to be around 25 nm. Fig.3.1(c) shows the TEM image of the nanocrystalline LCMO sample (calcined at 800 ^{o}C) in which the size of the clearly resolved grains is seen to be around 25 nm. The crystallite size for this sample determined by Rietveld analysis is ~25.8(1) nm which is in well agreement with the microscopic results. We also calculated the crystallite size of LCMO samples obtained at various calcination temperatures using Rietveld analysis. The crystallite sizes for the calcination temperatures 800, 900, 1000, 1100, 1200, 1300 and 1400 ^{o}C were obtained to be 25.8(1), 118.1(7), 216(3), 236(2), 272(3), 304(1) and 653(11) nm respectively. Fig. 3.1(d) shows the EDS spectrum for the nanocrystalline LCMO sample and the atomic percentage of the La, Ca and Mn determined from this spectrum. The result for the light oxygen atom is excluded in this calculation, as the EDS analysis does not give the accurate results for lighter atoms. The nominal composition for atomic percentage for Ca, Mn and La corresponds to 25, 50 and 25% respectively, when oxygen is excluded in the calculation.

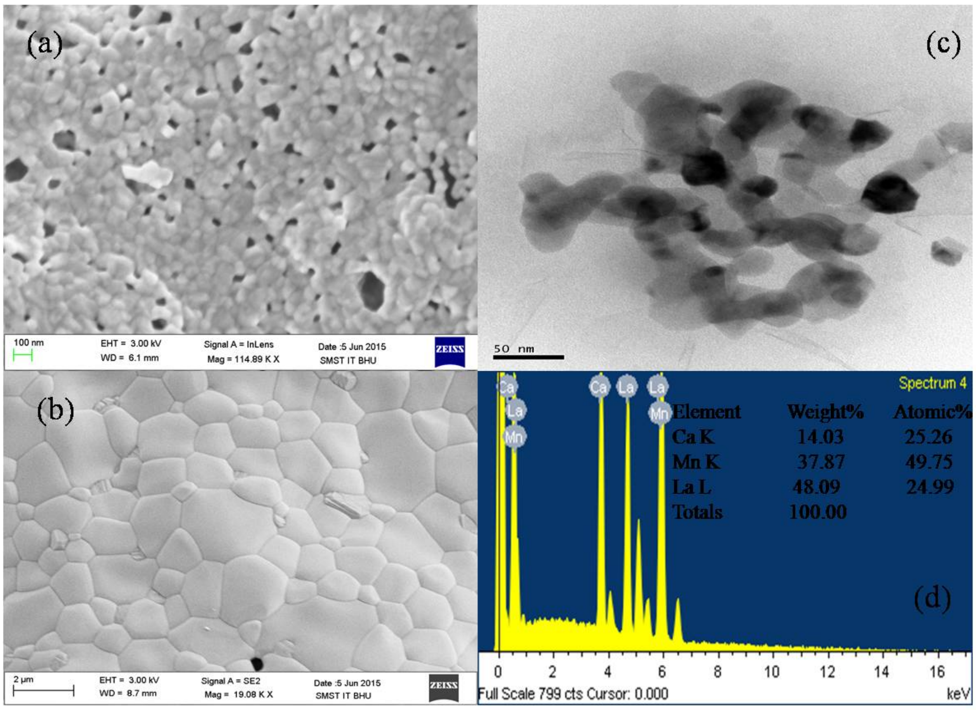

Element	Weight%	Atomic%
Ca K	14.03	25.26
Mn K	37.87	49.75
La L	48.09	24.99
Totals	100.00	

Fig. 3.1. SEM image of $La_{0.5}Ca_{0.5}MnO_3$ (a) calcined at 800 °C (b) calcined at 1400 °C (c) TEM Image of $La_{0.5}Ca_{0.5}MnO_3$ calcined at 800 °C (d) EDS of $La_{0.5}Ca_{0.5}MnO_3$ calcined at 800 °C.

The experimentally calculated atomic percentages for Ca, Mn and La are 25.26, 49.75 and 24.99 respectively which matches well with the nominal composition within the experimental error.

Fig. 3.2 shows the X-ray photoelectron spectra (solid circle) of Mn $^2P_{3/2}$ core level for nanocrystalline $La_{0.5}Ca_{0.5}MnO_3$ calcined at 800 ^{0}C. This spectrum exhibits a broad asymmetry curve due to presence of binding energy peaks for both the Mn^{3+} and Mn^{+4} ions. As reported for manganites by earlier authors [Markovich et al. (2008); Beyreuther et al. (2006); Plecenik et al. (2002)], we fitted the core level peak for the Mn^{+4} ions at ~643 eV (solid triangles) and for Mn^{+3} ion at ~641.4 eV (solid squares).The area under Mn^{+4} and Mn^{+3} peaks were used to analyze the relative fraction of these ions in our sample. The continuous line overlapping the observed (solid circles) XPS data corresponds to the resulting curve fit. The bottom curve (stars) in Fig. 3.2 shows Shirley background. We found equal proportion of the Mn^{+4} and Mn^{+3} ions by XPS analysis. Presence of oxygen nonstoichiometry is known to affect the valance state and relative proportion of the Mn ions to maintain the electro-neutrality [Symianakis et al. (2015)]. An oxygen rich sample will have higher Mn^{4+}/Mn^{3+} ratio than the nominal composition while the oxygen deficient sample will have Mn^{4+}/Mn^{3+} ratio lower than the nominal composition. As per the nominal composition of $La_{0.5}Ca_{0.5}MnO_3$ the Mn^{4+}/Mn^{3+} ratio should be one which is experimentally obtained for the LCMO sample calcined at 800 ^{o}C. This suggests that our sample has stoichiometric oxygen content.

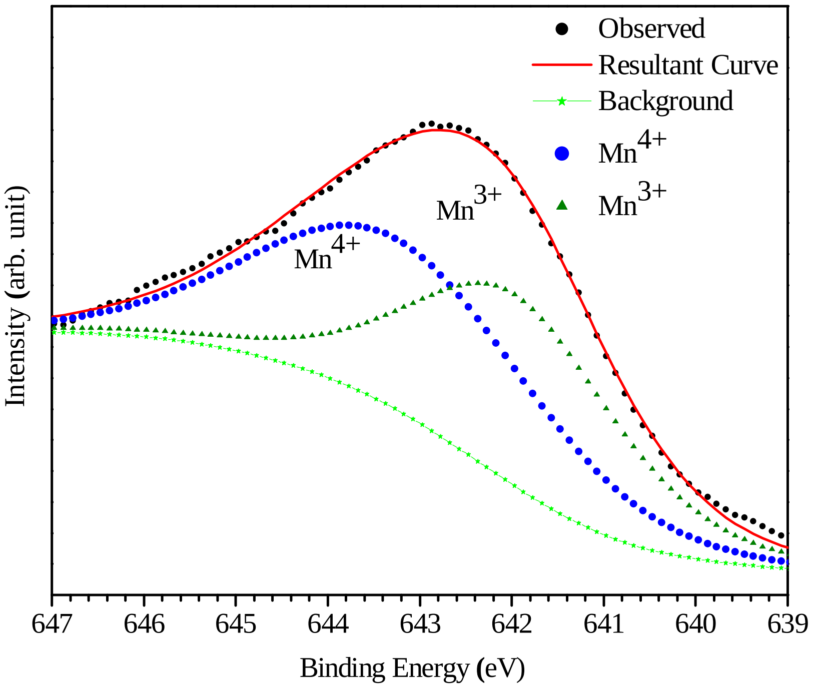

Fig. 3.2. X-ray photoelectron spectra (solid circles) of Mn $^2P_{3/2}$ core level for nanocrystalline $La_{0.5}Ca_{0.5}MnO_3$ calcined at 800 °C. The solid triangles and solid squares show the core level peak fits for the Mn^{3+} and Mn^{4+} ions, respectively. The bottom curve (stars) shows Shirley background. The continuous line overlapping the observed XPS data (solid circles) shows the resulting curve fit.

3.3.2 Rietveld Structural Analysis of Samples Prepared by Combustion Method

The structure of the bulk and nanocrystalline LCMO, NCMO and PCMO samples with various particle sizes were analyzed by Rietveld method. Rietveld analysis of the XRD data reveals that the structure of bulk as well as nanocrystalline samples of all the three manganites is orthorhombic in the *Pnma* space group. This is consistent with earlier reports of *Pnma* structure for these manganites in bulk as well as nanocrystalline forms [Zhang et al. (2009); Rao et al. (2006); Jirak et al. (2010); Sarkar et al. (2008); Martinelli et al. (2013)].

The crystallite/particle size for nano samples were calculated from the Rietveld method, providing the input file containing the instrumental resolution function; this input file was obtained using Si standard. The crystallite sizes obtained by Rietveld analysis are ~25.8(1), ~26.2(2) and ~28.1(1) nm for LCMO(C8), NCMO(C7) and PCMO(C8) samples, respectively.

Figs. 3.3, 3.4 and 3.5 show the Rietveld fits for the room temperature x-ray diffraction patterns of bulk and nanocrystalline LCMO, NCMO and PCMO samples respectively, using *Pnma* space group. The fit between the experimentally observed and Rietveld calculated diffraction profiles are quite good confirming the orthorhombic structure of these manganites for both the bulk and nanocrystalline samples. The refined structural parameters and agreement factors are given in table 3.1, 3.2 and 3.3 for LCMO, NCMO and PCMO respectively.

Table 3.1. Refined structural parameters obtained from the Rietveld refinement of the room temperature structure of $La_{0.5}Ca_{0.5}MnO_3$ samples calcined at 600 ^{o}C, 800 ^{o}C and 1400 ^{o}C.

Parameters	LCMO (C1400) (Bulk) *Pnma*	LCMO (C800) (Nano) *Pnma*	LCMO (C600) (Nano) *Pnma*
a(Å)	5.4166(2)	5.4219(1)	5.461(1)
b(Å)	7.6409(3)	7.643(2)	7.667(2)
c(Å)	5.4277(2)	5.451(1)	5.490(1)
V(Å^3)	224.64(1)	225.44(6)	229.91(1)
(La, Ca) (x,y,z)	{0.0172(3),1/4,0.4986(8)}	{0.0108(6),1/4,0.497(1)}	{0.007(1),1/4,0.496(1)}
B(Å^2)	1.04(2)	0.31(1)	0.14 (2)
Mn(x,y,z)	{0,0,0}	{0,0,0}	{0,0,0}
B(Å^2)	0.85(4)	0.621(2)	0.645(1)
O(1) (x,y,z)	{0.491(2),1/4,0.565(2)}	{0.458(4),1/4,0.582(4)}	{0.452(7),1/4,0.594(5)}
B(Å^2)	0.2(3)	0.485(1)	0.697(2)
O(2) (x,y,z)	{0.279(3),0.032(1),0.221(3)}	{0.272(4),0.019(3),0.230(3)}	{0.24(1),0.018(4),0.24(1)}
B(Å^2)	1.4(2)	0.71(3)	0.92 (1)
χ^2	1.51	1.35	1.80
Mn-O(1)(Å)	1.9431	1.9454	2.0022
Mn-O(2)(Å)	1.9449	1.9284	1.8636
Mn-O(2)$^{/}$(Å)	1.9458	1.9757	2.0181
Mn-O(1)-Mn(^{o})	158.88	150.59	146.39
Mn-O(2)-Mn(^{o})	160.44	167.10	171.83

Table 3.2. Refined structural parameters obtained from the Rietveld refinement of the room temperature structure of $Nd_{0.5}Ca_{0.5}MnO_3$ calcined at 700 ^{o}C, 900 ^{o}C and 1100 ^{o}C.

Parameters	NCMO (C1100) (Bulk) *Pnma*	NCMO (C900) (Nano) *Pnma*	NCMO (C700) (Nano) *Pnma*
a(Å)	5.3784(2)	5.3711(8)	5.344(1)
b(Å)	7.5979(8)	7.6071(5)	7.646(1)
c(Å)	5.3953(4)	5.3980(7)	5.403(1)
V(Å^3)	220.48(3)	220.53(4)	220.85(9)
(Nd, Ca) (x,y,z)	{0.0301(2),1/4,0.4952(9)}	{0.0305(2),1/4,0.4939(8)}	{0.0255(6),1/4,0.504(1)}
B(Å^2)	0.06(3)	0.35(1)	0.28(3)
Mn(x,y,z)	{0,0,0}	{0,0,0}	{0,0,0}
B(Å^2)	0.41(4)	0.14(3)	0.13(6)
O(1) (x,y,z)	{0.488(1),1/4,0.577(3)}	{0.490(1),1/4,0.579(3)}	{0.472(3),1/4,0.524(8)}
B(Å^2)	0.4(4)	0.4(3)	0.5(6)
O(2) (x,y,z)	{0.292(2),0.031(1),0.219(2)}	{0.297(2),0.028(1),0.216(2)}	{0.31(4),0.054(1),0.219(4)}
B(Å^2)	0.3(2)	0.2(2)	0.9(4)
χ^2	1.25	1.42	1.66
Mn-O(1)(Å)	1.9463	1.9479	1.9217
Mn-O(2)(Å)	1.8928	1.8902	1.9291
Mn-O(2)$^{/}$(Å)	1.9893	1.9869	2.1201
Mn-O(1)-Mn(^{o})	155.11	156.65	168.17
Mn-O(2)-Mn(^{o})	158.33	157.71	148.26

Table 3.3. Refined structural parameters obtained from the Rietveld refinement of the room temperature structure of $Pr_{0.5}Ca_{0.5}MnO_3$ calcined at 700 ^oC, 900 ^oC and 1100 ^oC.

Parameters	PCMO (C1100) (Bulk) *Pnma*	PCMO (C900) (Nano) *Pnma*	PCMO (C700) (Nano) *Pnma*
a(Å)	5.3948(5)	5.3952(5)	5.399(1)
b(Å)	7.6302(9)	7.6383(4)	7.641(1)
c(Å)	5.4085(4)	5.4138(3)	5.415(1)
V(Å^3)	222.41(3)	222.50(2)	223.54(7)
(Pr, Ca) (x,y,z)	{0.0269(2),1/4,0.4961(9)}	{0.0268(2),1/4,0.5067(5)}	{0.0246(4),1/4,0.499(1)}
B(Å^2)	0.16(3)	0.21(2)	0.24(2)
Mn(x,y,z)	{0,0,0}	{0,0,0}	{0,0,0}
B(Å^2)	0.32(1)	0.18(1)	0.17(4)
O(1) (x,y,z)	{0.490(1),1/4,0.571(4)}	{0.492(1),1/4,0.548(5)}	{0.488(2),1/4,0.551(4)}
B(Å^2)	0.6(6)	0.49(1)	0.7(6)
O(2) (x,y,z)	{0.284(2),0.033(2),0.219(2)}	{0.288(2),0.035(1),0.218(2)}	{0.291(3),0.04(2),0.225(3)}
B(Å^2)	0.28(3)	1.49(1)	1.1(4)
χ^2	2.23	2.62	2.15
Mn-O(1)(Å)	1.949	1.951	1.932
Mn-O(2)(Å)	1.937	1.919	1.918
Mn-O(2)$^{/}$(Å)	1.951	1.971	1.996
Mn-O(1)-Mn(^{o})	157.07	163.33	164.15
Mn-O(2)-Mn(^{o})	159.02	157.62	156.55

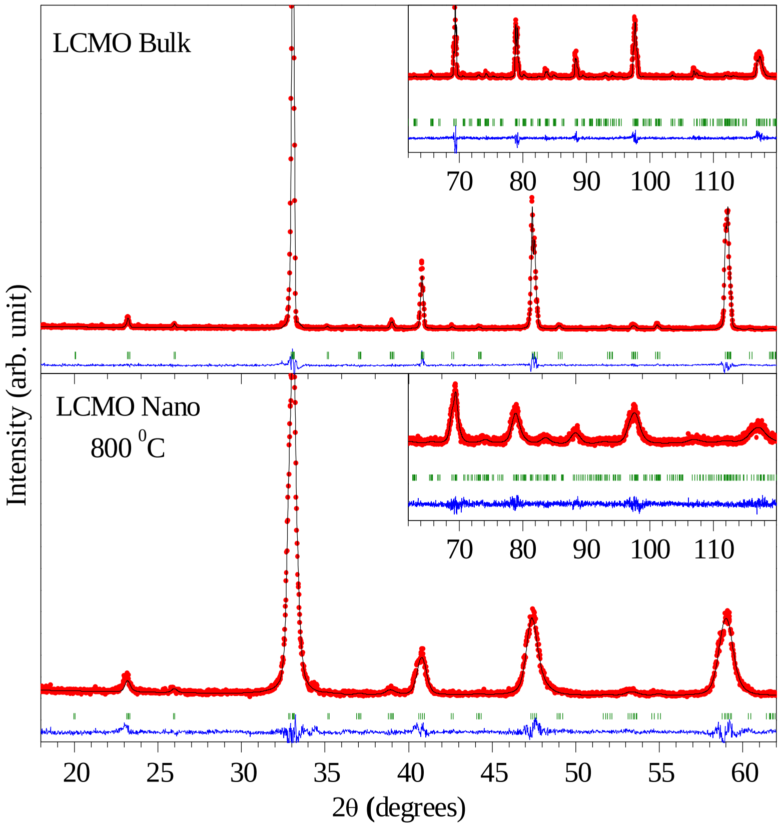

Fig. 3.3. Experimentally observed (dots), Rietveld calculated (continuous line) and their difference (continuous bottom line) profiles for bulk and nanocrystalline $La_{0.5}Ca_{0.5}MnO_3$, samples obtained after Rietveld analysis of the XRD data using orthorhombic space group *Pnma*. The vertical tick marks between the observed and difference plot show the Bragg peak positions.

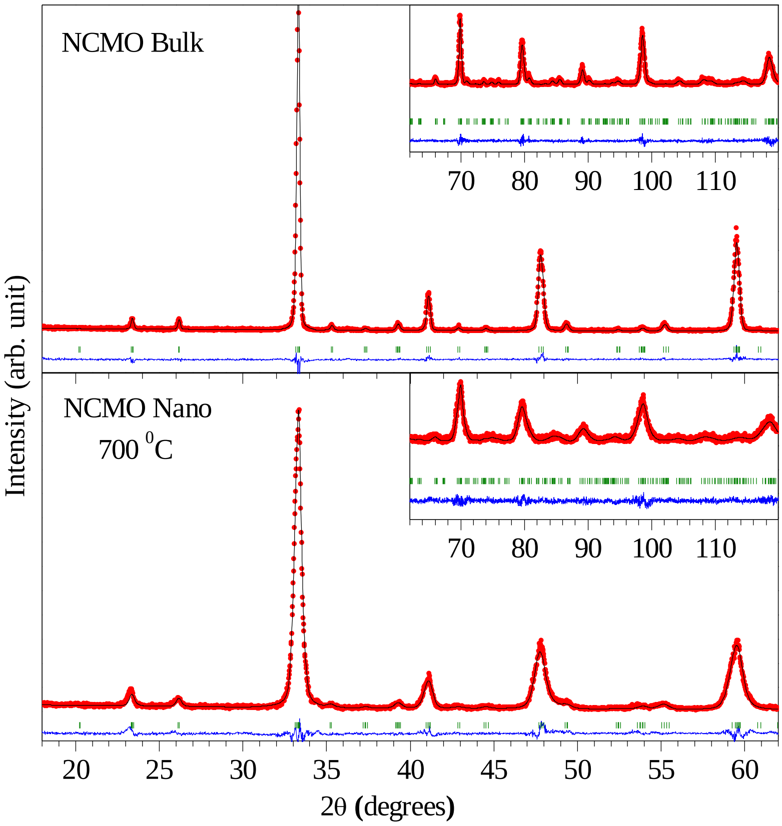

Fig. 3.4. Experimentally observed (dots), Rietveld calculated (continuous line) and their difference (continuous bottom line) profiles for bulk and nanocrystalline $Nd_{0.5}Ca_{0.5}MnO_3$ samples obtained after Rietveld analysis of the XRD data using orthorhombic space group *Pnma*. The vertical tick marks between the observed and difference plot show the Bragg peak positions.

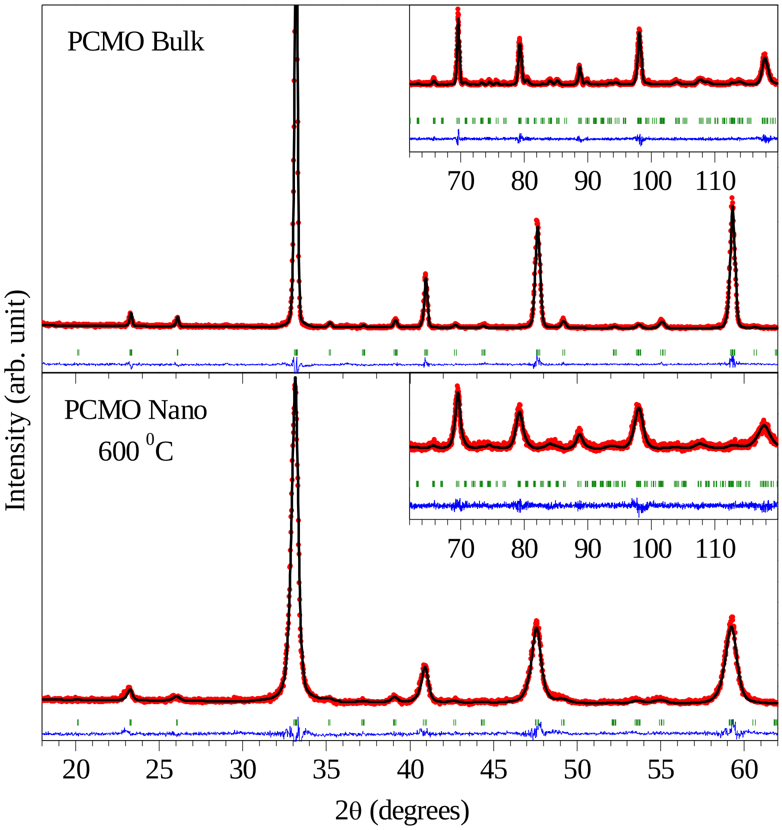

Fig. 3.5. Experimentally observed (dots), Rietveld calculated (continuous line) and their difference (continuous bottom line) profiles for bulk and nanocrystalline $Pr_{0.5}Ca_{0.5}MnO_3$ samples obtained after Rietveld analysis of the XRD data using orthorhombic space group *Pnma*. The vertical tick marks between the observed and difference plot show the Bragg peak positions.

The refined structural parameters for bulk samples are in well agreement with the earlier reports [Rao et al. (2006); Jirak et al. (2010); Radaelli et al. (1997)]. Evolution of the unit cell volumes with crystallite size, as obtained from the Rietveld analysis of the XRD data for LCMO, NCMO and PCMO, is shown in Fig. 3.6(a), (b) and (c) respectively. As can be seen from Fig. 3.6 the unit cell volume consistently increases with decreasing the particle size/calcination temperature for all the three manganites. We show in Fig. 3.7, the strongest perovskite peak around ($2\theta \approx 33$) in the x-ray diffraction pattern of LCMO, NCMO and PCMO samples calcined at various temperatures to further confirm this observation. With decreasing calcination temperature and particles size, shift of XRD peak towards lower angle is clearly seen for the LCMO and NCMO samples, implying increasing unit cell volume. For the PCMO samples the shift in the XRD peaks is not very clear perhaps due to anisotropic stain in the nano samples. The unit cell volume of the LCMO14 calcined at 1400 ^{o}C is found to be 224.64 Å^{3} which is in well agreement with that reported by Jirak et al. (2010) (224.96 Å^{3}) and Sarkar et al. (2008) (224.7 Å^{3}). The unit cell volume of the LCMO bulk sample reported by Radaelli et al. (1997) is slightly higher (22.48 Å^{3}) but their sample was prepared by solid state method and not the wet chemical route. The unit cell volume of the LCMO (C6) and LCMO (C8) samples are 229.91 Å^{3} and 225.45 Å^{3} respectively which are significantly higher than the bulk one. Jirak et al. (2010) have also reported larger unit cell volume (225.96 Å^{3}) for the LCMO sample prepared by modified sol-gel method and calcined at 700 ^{o}C. The unit cell volume of LCMO reported by Sarkar et al. (2008), for the LCMO nano sample prepared by sol-gel method and heat treated at 750 ^{o}C, is 221.5 Å^{3} which is significantly less than the bulk.

In contrast, for $La_{2/3}Ca_{1/3}MnO_3$, Sarkar et al. (2008), reported that the unit cell volume of the nano samples is larger than the bulk. Iniama et al. (2014) reported that the unit cell volume is 221.6 Å^3 for the nano LCMO sample prepared by sol-gel method and heat treated at 800 ^{o}C. The unit cell volume for the nano sample prepared by us using sol-gel method and heat treated at 800 ^{o}C also comes out to be 223.87 Å^3 which is lower than the bulk one. The reason for lower unit cell volume of these samples is discussed in section 3.3.5 and 3.4. In case of NCMO sample the unit cell volume of the bulk (calcined at 1100 ^{o}C) and nano (calcined at 700 ^{o}C) samples are obtained to be 220.48 Å^3 and 220.85 Å^3. Again the unit cell volume is higher for the nano sample. This is in agreement with that reported by Rao et al. (2006) as 220.97 Å^3 for nano (calcined at 600 ^{o}C) and 219.61 Å^3 for bulk (calcined at 900 ^{o}C) samples. The unit cell volume for the bulk NCMO sample reported by Richard et al. (1999) is 220.85Å^3 which matches with our result. The unit cell volume for the bulk and nano PCMO samples are found to be 222.63 Å^3 (calcined at 1100 ^{o}C) and 223.46 Å^3 (calcined at 700 ^{o}C) respectively. The unit cell volume for the bulk (calcined at 1200 ^{o}C) PCMO sample reported by Jirak et al. (2010) is 222.02 Å^3 while that for the nano (calcined at 700 ^{o}C) sample is 222.36 Å^3. The bulk unit cell volume for the NCMO sample sintered at 1500 ^{o}C is reported to be 221.77 Å^3 [Jirak et al. (2010)]. This again confirms that the unit cell volume for the samples heat treated at lower temperatures is higher than that at higher temperatures with larger particle sizes.

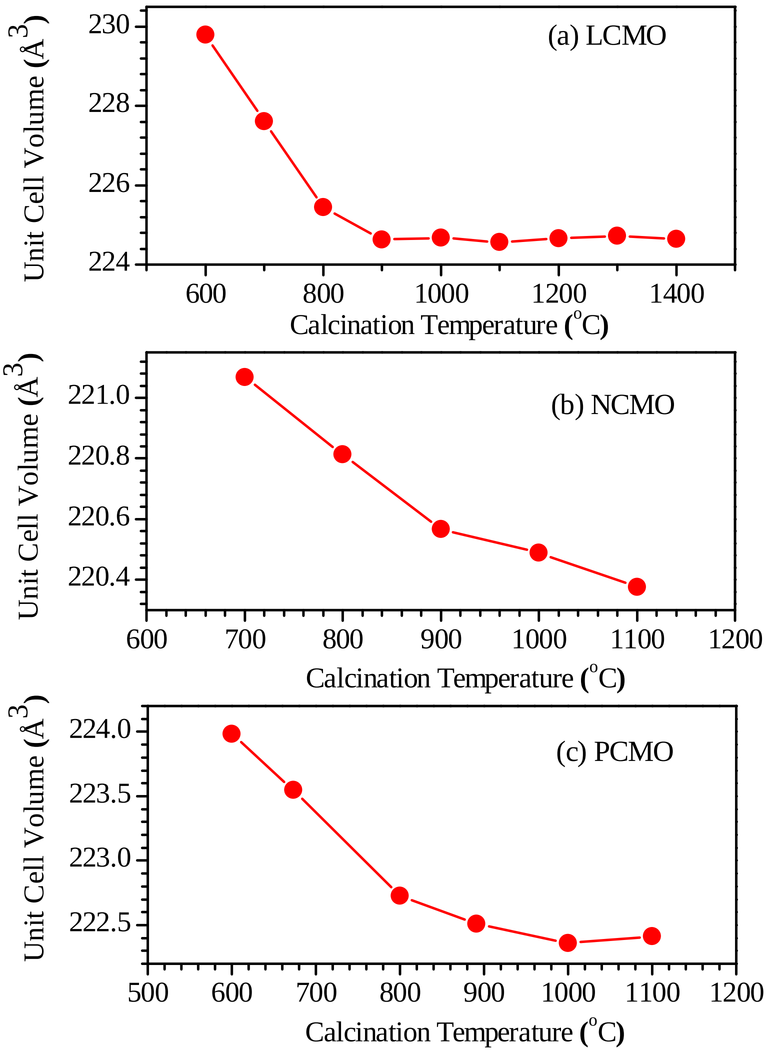

Fig. 3.6. Evolution of the unit cell volume for bulk and nanocrystalline $La_{0.5}Ca_{0.5}MnO_3$, $Nd_{0.5}Ca_{0.5}MnO_3$ and $Pr_{0.5}Ca_{0.5}MnO_3$ samples calcined at various temperatures.

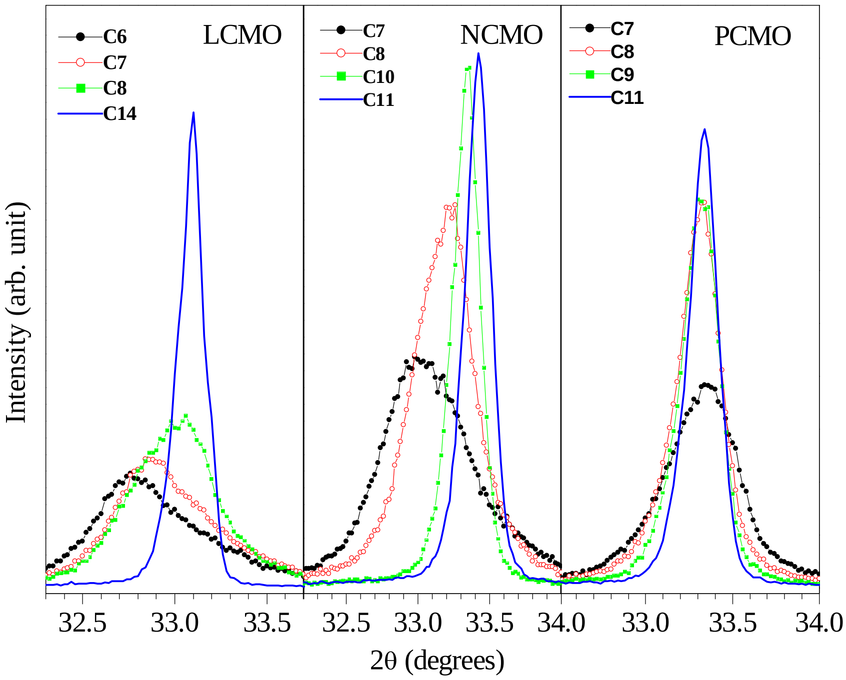

Fig. 3.7. Evolution of strongest XRD profile for bulk and nanocrystalline $La_{0.5}Ca_{0.5}MnO_3$, $Nd_{0.5}Ca_{0.5}MnO_3$ and $Pr_{0.5}Ca_{0.5}MnO_3$ samples calcined at various temperatures. The samples calcined at 600, 700, 800, 900, 1000, 1100, 1200, 1300 and 1400 ^{o}C are denoted as C6, C7, C8, C9, C10, C11, C12, C13 and C14 respectively.

Fig.3.8 (a), (b) and (c), depicts the variation of lattice parameters with calcination temperature, for LCMO, NCMO and PCMO respectively. For LCMO, the ‘a’, ‘b’ and ‘c’ parameters are distinct with $b/\sqrt{2}<a<c$ similar to that reported by earlier authors. In contrast, for NCMO and PCMO, the $b/\sqrt{2}$ and c parameters are very close for nanocrystalline samples. We checked if a tetragonal structure can account for the diffraction pattern of the nano samples of NCMO and PCMO. However, consideration of tetragonal I*4*/mcm space group in Rietveld structure refinement could not account for many superlattice reflections which are indexed in the *Pnma* space group. Thus the structure of nano NCMO and PCMO samples are indeed orthorhombic in the *Pnma* space group. For LCMO, the lattice parameters ‘a’, ‘$b/\sqrt{2}$’ and ‘c’ continuously increase with decreasing particle size. As shown in Fig. 3.6b, in case of NCMO, the lattice parameter ‘$b/\sqrt{2}$’ and ‘a’ increases while ‘c’ parameter decreases with decreasing calcination temperature/particle size. The ‘c’ and ‘$b/\sqrt{2}$’ parameters of PCMO increase continuously with decreasing calcination temperature/particle size while ‘a’ parameter first decreases slightly and then increases (see Fig. 3.8c).

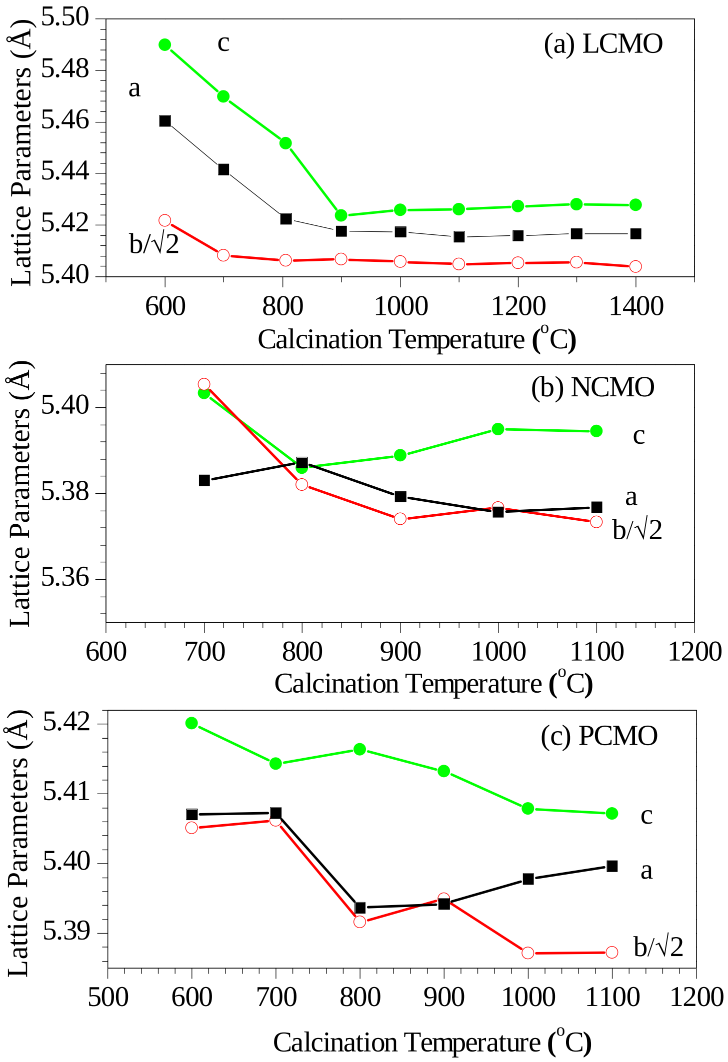

Fig. 3.8. Evolution of lattice parameters for bulk and nanocrystalline samples calcined at various temperatures (a) $La_{0.5}Ca_{0.5}MnO_3$ (b) $Nd_{0.5}Ca_{0.5}MnO_3$ and (c) $Pr_{0.5}Ca_{0.5}MnO_3$.

We also analyzed the orthorhombic strain $OS_{\perp}$ and $OS_{||}$ for the LCMO, NCMO and PCMO samples calcined at various temperatures which is shown in Fig. 3.9. The orthorhombic strains $OS_{||} = 2\frac{(c-a)}{(c+a)}$ gives the strain in the ac plane, while $OS_{\perp} = 2\frac{(c+a-b\sqrt{2})}{(c+a+b\sqrt{2})}$ along the b axis. As reported by earlier authors also [Zhou et al. (2013); Giri et al. (2011); Sarkar et al. (2008)], for LCMO, the orthorhombic strains are small in bulk samples with $OS_{\perp} > OS_{||}$. In case of both the LCMO and NCMO the orthorhombic strains significantly increases for the nanocrystalline samples. In case of PCMO the orthorhombic strains are significantly small and show insignificant change with changing particle size. It is reported for the bulk sample of LCMO [Sarkar et al. (2009)] that the $OS_{\perp}$ significantly increases in the low temperature charged ordered phase. Since the orthorhombic strains are significantly high for the nano samples at room temperature itself decreasing temperature does not lead to any further enhancement [Sarkar et al. (2009)] with the consequence that the room temperature ferromagnetic phase remains stable down to low temperatures. Significantly larger orthorhombic strains in nano samples than the bulk LCMO is also reported by Sarkar et al. (2009).

3.3.3 Variation of Mn-O Bond Lengths with Crystallite Size

To correlate the increased unit cell volume of the nano samples with the structural changes at atomic level and find out the reason for suppression of charge ordering transition, we investigated the variation of Mn-O bond lengths with calcination temperature/particle size. The variation of Mn-O bond lengths and bond angles with calcination temperature of the samples is shown in Fig. 3.10(a-c).

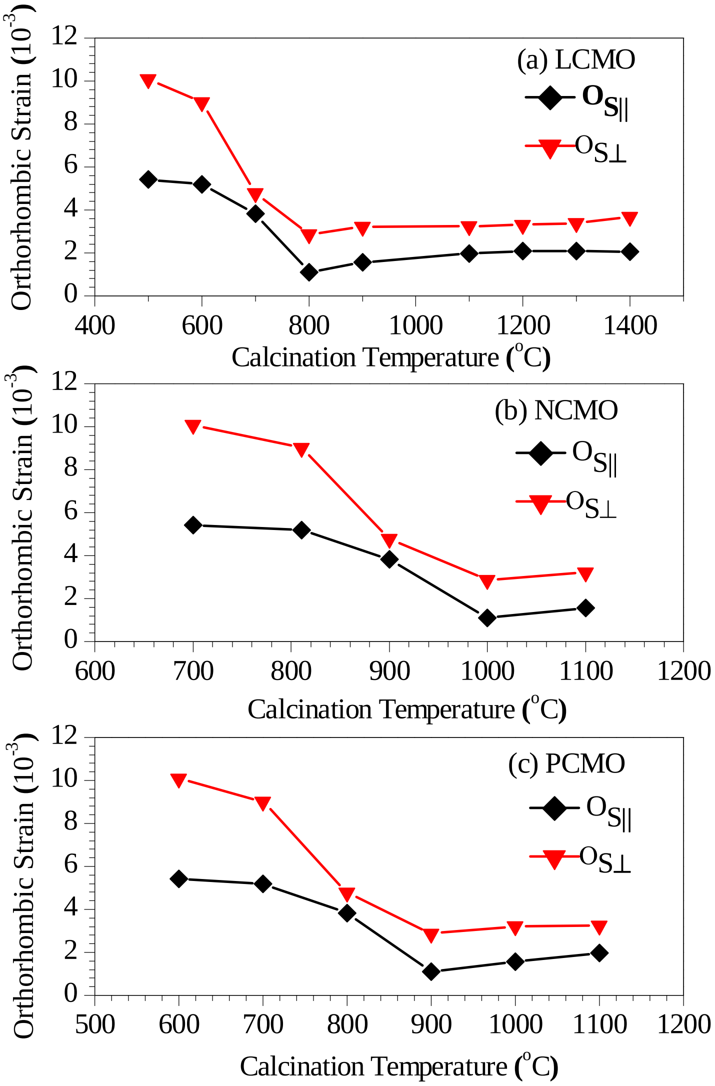

Fig. 3.9. Variation of orthorhombic strain $OS_{\perp}$ (perpendicular strain along the b- axis) and $OS_{\parallel}$ (strain in ac– plane) for bulk and nanocrystalline samples calcined at various temperatures (a) $La_{0.5}Ca_{0.5}MnO_3$ (b) $Nd_{0.5}Ca_{0.5}MnO_3$ and (c) $Pr_{0.5}Ca_{0.5}MnO_3$.

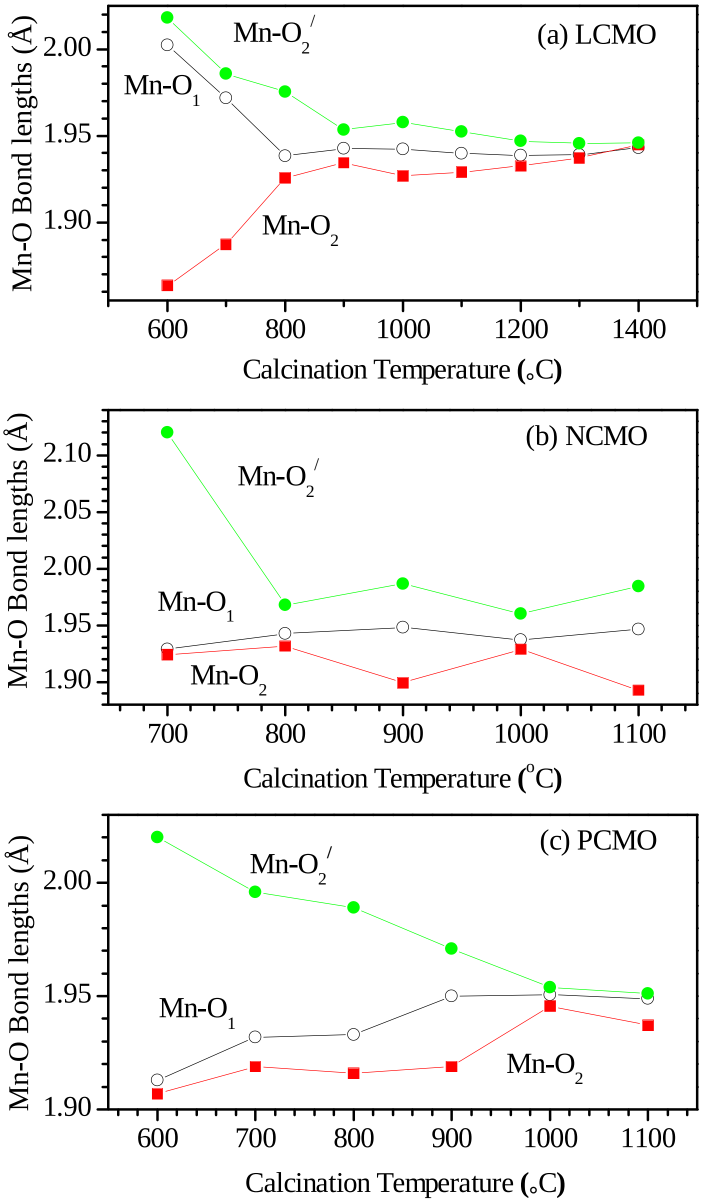

Fig. 3.10. Variation of Mn-O Bond lengths for (a) $La_{0.5}Ca_{0.5}MnO_3$ (b) $Nd_{0.5}Ca_{0.5}MnO_3$ and (c) $Pr_{0.5}Ca_{0.5}MnO_3$ samples calcined at various temperatures.

As can be seen from this figure, for nano samples one of the Mn-O_2 bond length is significantly decreased while Mn-O_1 and other Mn-O_2 bond lengths are enhanced. A Similar variation of bond lengths are reported in the bulk samples of $La_{0.75}Ca_{0.25}MnO_3$ in the stability region of ferromagnetic phase at lower temperatures [Radaelli et al. (1996)]. Since the bond lengths for ferromagnetic ground state are already met in nanocrystalline samples they are expected to remain unchanged by decreasing temperature thereby inhibiting the appearance of charge ordered phase. Also, similar changes in bond length are reported as a function of oxygen off-stoichiometry (δ) at room temperature in bulk samples of $LaMnO_{3+\delta}$ series where the ferromagnetic phase is stabilized [Ritter et al. (1997); Woodward et al. (1999); Cortes-Gil et al. (2012)]. Thus the structural parameters for the nanocrystalline LCMO, NCMO and PCMO favor the stability of ferromagnetic phase and there will not be any phase transition in such samples when they will be cooled below room temperature. This is exactly the case with the nanocrystalline LCMO, PCMO and NCMO samples that retain the room temperature *Pnma* structure and ferromagnetic metallic state well below the room temperature.

3.3.4 Magnetic Measurements

The magnetization (M) versus temperature (T) data in the zero field cooling (ZFC) and field cooling field warming (FCW) measurements taken on the bulk and nanocrystalline LCMO samples are shown in Fig. 3.11 at two fields (0.05T and 1T).

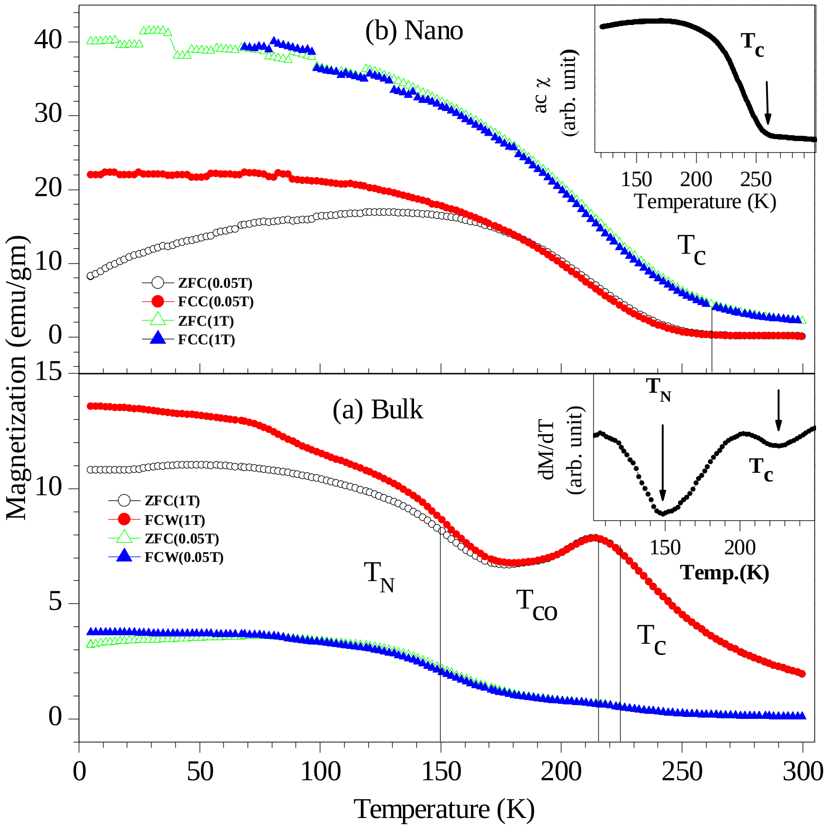

Fig. 3.11. Magnetization (M) vs temperature (T) curve measured at 0.05 T and 1 T magnetic fields for (a) bulk $La_{0.5}Ca_{0.5}MnO_3$ sample (lower panel) and nano $La_{0.5}Ca_{0.5}MnO_3$ sample calcined at 800 ^{O}C (upper panel). Inset to figure (a) shows first order derivative of magnetization (M) with respect to temperature (T) for bulk $La_{0.5}Ca_{0.5}MnO_3$ sample. Inset to figure (b) shows ac-susceptibility vs temperature for nanocrystalline $La_{0.5}Ca_{0.5}MnO_3$ sample calcined at 800 ^{o}C.

As shown in Fig. 3.11(a) the bulk sample shows transition from paramagnetic to ferromagnetic state at $T_C \approx 225$ K due to which magnetization rises and then on further cooling transition to charge ordered state at $T_{CO} \approx 215$ K and finally to antiferromagnetic phase at $T_N \approx 150$ K. These transition temperatures are more clearly seen in temperature versus dM/dT plot for ZFC measurements at 0.05T field as shown in inset to Fig. 3.11(a). Similar $T_C \approx 225$K and $T_N \approx 155$ K values are reported for bulk LCMO by earlier authors [Radaelli et al. (1997); Hung et al. (2000)]. At lower temperatures and low field (≈ 0.05T) there is clear separation of the zero field cooled (ZFC) and field cooled data, which occurs close to temperature where the magnetization shows the peak. This is attributed to the irreversibility that may arise due to remanant spin disorder in sample [Jirak et al. (2010)]. In contrast to the bulk sample, the nanocrystalline sample does not show antiferromagnetic transition below the transition from paramagnetic to ferromagnetic state at $T_C \approx 260$K as shown in Fig. 3.11(b). The inset to Fig. 3.11(b) shows the temperature (T) versus ac-susceptibility (χ) data for the nano LCMO sample. As can be seen from this figure there is rise in the ac-susceptibility (χ) around 260K corresponding to paramagnetic to ferromagnetic transition. This is in well agreement with the T_C reported by Jirak et al. (2010) for nano crystalline LCMO sample. Similar to our result, earlier authors also reported gradual increase in the susceptibility below T_C for the nano samples [Jirak et al. (2010); Sarkar et al. (2008)]. The magnetization of nanocrystals at 1T rises monotonically (for both FC and ZFC) and approaches toward saturation at the lowest temperature. The M-T measurements on nano LCMO sample is in good agreement with the results of earlier authors [Jirak et al. (2010); Sarkar et al. (2008)].

In Fig. 3.12 we show the magnetization (M) vs. magnetic field (H) curves for the LCMO bulk and nanocrystalline samples measured at 5K. In comparison to bulk sample which shows no hysteresis in the M-H loop, the nanocrystalline sample shows considerable hysteresis with a coercive field of ~ 0.048T and remanent magnetization of ~ 18 emu/gm. In contrast there is no remanent magnetization or coercive field in the bulk sample. Similar M-H loop for the bulk LCMO sample were reported by earlier authors [Jirak et al. (2010); Sarkar et al. (2008)]. The M-H data clearly show that the nanocrystals retain their room temperature ferromagnetic state as they are cooled to lower temperatures unlike the bulk sample that exhibit the antiferromagnetic transition. Inset to Fig. 3.12 shows the M-H curve at room temperature for LCMO bulk and nanocrystalline samples demonstrating the paramagnetic state for both the samples. The value of magnetization calculated at highest field 5T for nano sample at 5 K is ~ 1.6 Bohr magnetons (μ_B) per formula unit, compared to expected value of 3.5 μ_B for Mn only ordering. Thus the magnetization of the nano sample is reduced by about 46% than theoretically expected value suggesting that whole sample is not ferromagnetic. Jirak et al. (2010) also have reported magnetic moment reduction of 50-60% in the 25 nm LCMO particles. Reduced magnetic moment of the magnetic nanoparticle and absence of saturation of M-H loop even at very high field is explained in terms of magnetic core and nonmagnetic shell [Jirak et al. (2010); Sarkar et al. (2008)].

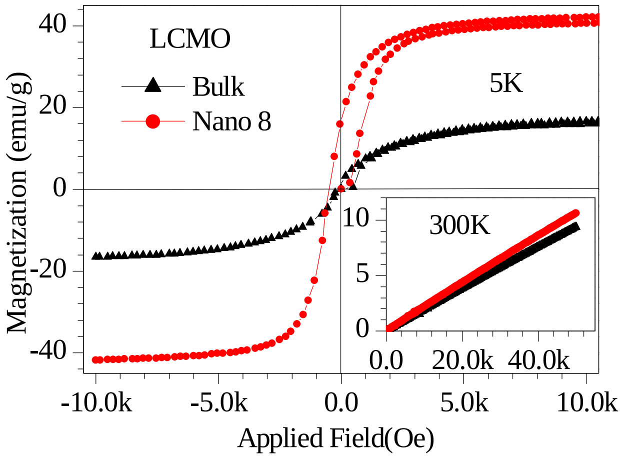

Fig. 3.12. Magnetization (M) versus applied magnetic field (H) plot for bulk and nanocrystalline (calcined at 800 ^{O}C) $La_{0.5}Ca_{0.5}MnO_3$ samples measured at 5 K (main panel) and at room temperature (RT) (inset). Ferromagnetic hysteresis loop is clearly seen for nano sample at 5 K. Inset shows the paramagnetic state for both the samples at 300 K (RT).

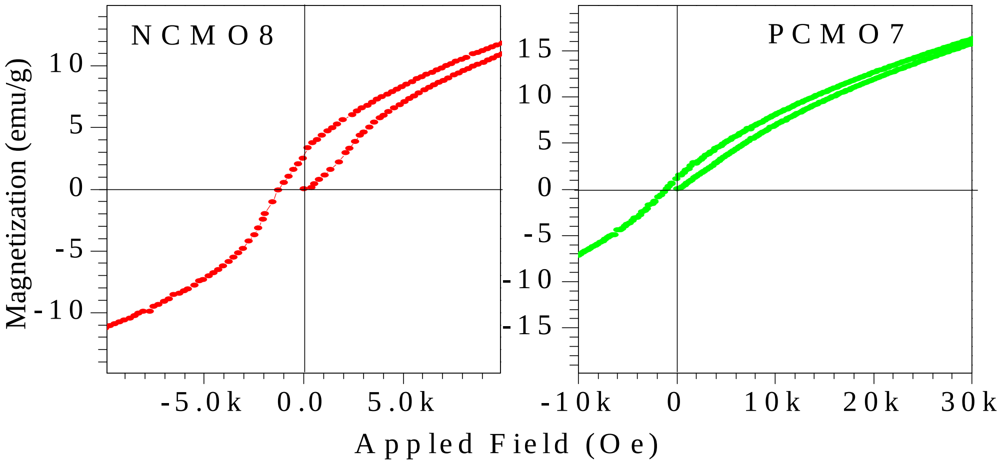

Fig. 3.13. Magnetization (M) versus applied magnetic field (H) plot for nanocrystalline $Nd_{0.5}Ca_{0.5}MnO_3$ (left panel) and $Pr_{0.5}Ca_{0.5}MnO_3$ (right panel) at 5 K. Ferromagnetic hysteresis loop is clearly seen for both the samples.

The M-H curve for the nanocrystalline NCMO and PCMO samples measured at 5K is given in the Fig. 3.13. As can be seen from this figure, NCMO and PCMO samples also exhibit ferromagnetic loop for nano samples. Thus we may conclude that the antiferromagnetic charge ordered state is absent in nano samples of LCMO, NCMO and PCMO in nanocrystalline form.

3.3.5 Rietveld Structural Analysis of LCMO Samples Prepared by sol-gel Method

It is clear from the foregoing discussion that the nanocrystalline LCMO, PCMO and NCMO samples have significantly higher unit cell volume than the bulk samples and retain their ferromagnetic state down to 5K temperature suggesting absence of charge ordering transition. We attribute this phenomenon to the increased bandwidth consequent upon increased unit cell volume in the nanocrystalline samples. Now one may ask why the nanocrystalline LCMO samples reported by Sarkar et al. (2008), also exhibits suppression of charge ordering transition even though the unit cell volume is significantly lower for the nano samples than the bulk. To find out the answer, we prepared another batch of LCMO samples following the same method as used by Sarkar et al. (2008). To our utmost surprise, we find that the nanocrystalline samples prepared by this method have significantly lower unit cell volume than the bulk. The Rietveld fit in Fig. 3.14, using orthorhombic *Pnma* space group for the XRD pattern of our sol-gel derived nanocrystalline sample recorded at room temperature and 15K reveals that there is no charge ordering transition in this sample also similar to the report of Sarkar et al. (2008).

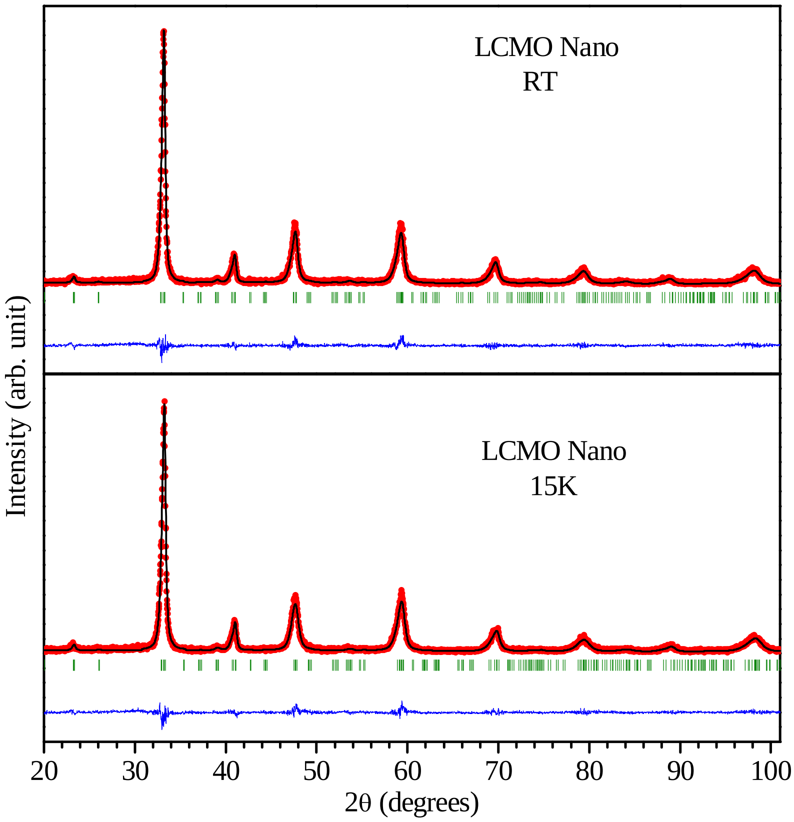

Fig. 3.14. Experimentally observed (dots), Rietveld calculated (continuous line) and their difference (continuous bottom line) profiles for nanocrystalline $La_{0.5}Ca_{0.5}MnO_3$, samples (prepared by Sol-Gel method and calcined at 700 ^{o}C) obtained after Rietveld analysis of the XRD data using orthorhombic space group Pnma. The vertical tick marks between the observed and difference plot show the Bragg peak positions. Upper panel at room temperature and lower panel at 15 K.

However, unlike the results of Sarkar et al. (2008), the unit cell volume decreases further with increasing calcination temperature (upto 1000 ^{o}C) and crystallite size [See top left panel of Fig. 3.15]. Variation of lattice parameter with calcination temperature is shown in lower left panel of Fig. 3.15. For calcinations temperature above 1000 ^{o}C, the unit cell volume starts increasing with increasing calcination temperature/particle size. Similar trend in the variation of the unit cell volume with calcination temperature/particle size has been recently reported by Iniama et al. (2014). To find out the possible reasons for this anomalous variation of unit cell volume with the calcination temperature/particle size, we examined the XRD patterns of these samples more carefully. We find that with increasing calcination temperature precipitation of Mn_3O_4 phase from the sol-gel derived LCMO sample takes place. Evolution of the strongest XRD peak [2theta=36.17] of Mn_3O_4 in the LCMO samples prepared by sol-gel method and calcined at various temperatures is shown in middle panel of Fig 3.15. The same angular range is shown in the right panel for the combustion synthesized samples to elucidate that there is no Mn_3O_4 impurity. The superlattice peak from the perovskite phase close to this position appears at 2theta=35.20, which makes it possible to unambiguously determine the evolution of the Mn_3O_4 impurity with temperature. It is evident from this figure that the intensity of the Mn_3O_4 impurity peak first increases with increasing calcination temperature upto 1000 ^{o}C and then starts decreasing. This suggests that above 1000 ^{o}C the Mn_3O_4 starts dissolving back to the LCMO. The precipitation of Mn_3O_4 from the nanocrystalline LCMO and its dissolution back to the matrix above 1000 ^{0}C is responsible for the anomalous variation of unit cell volume with calcination temperature/particle size. It is reported for $LaMnO_3$ that off stoichiometry can significantly decrease the unit cell volume and stabilize the ferromagnetic state in the otherwise antiferromagnetic state for the stoichiometric compound [Ritter et al. (1997)]. The unit cell volume of stoichiometric $LaMnO_3$ (magnetic state antiferromagnetic) is reported to be 243.84 $Å^3$ which may decrease upto 230.04 $Å^3$ for nonstoichiometric $La_{0.952}Mn_{0.952}O_3$ thereby stabilizing ferromagnetic magnetic state for this sample [Woodward et al. (1999)]. The significant enhancement in the unit cell volume of our samples prepared by combustion method suggests that they are stoichiometric and increment of the unit cell volume is caused by size effect. The unit cell volume of our sol-gel derived sample calcined at 600 ^{o}C is ~224.55 $Å^3$ which is close to the unit cell volume of the bulk sample prepared by us using combustion method and the bulk sample of Sarkar et al. (2008) prepared by sol-gel method. If our sol gel derived sample has been stoichiometric then its unit cell volume should have been higher similar to the sample prepared by the combustion method. With increasing calcination temperature upto 1000 ^{o}C, the sample becomes more nonstoichiometric because of the precipitation of Mn_3O_4 and consequently the unit cell volume decreases. For calcination temperature above 1000 ^{o}C the stoichiometry and the unit cell volume of the sample is restored by dissolution of the Mn_3O_4 precipitate. As pointed out by Iniama et al. (2014), the unit cell volume decreases with increasing crystallite size in the size range of 15 to 22 nm which has not been investigated by Sarkar et al. (2008). Sarkar et al. (2008) have attributed the lower unit cell volume for smaller crystallite size samples to the hydrostatic pressure caused by excess surface energy.

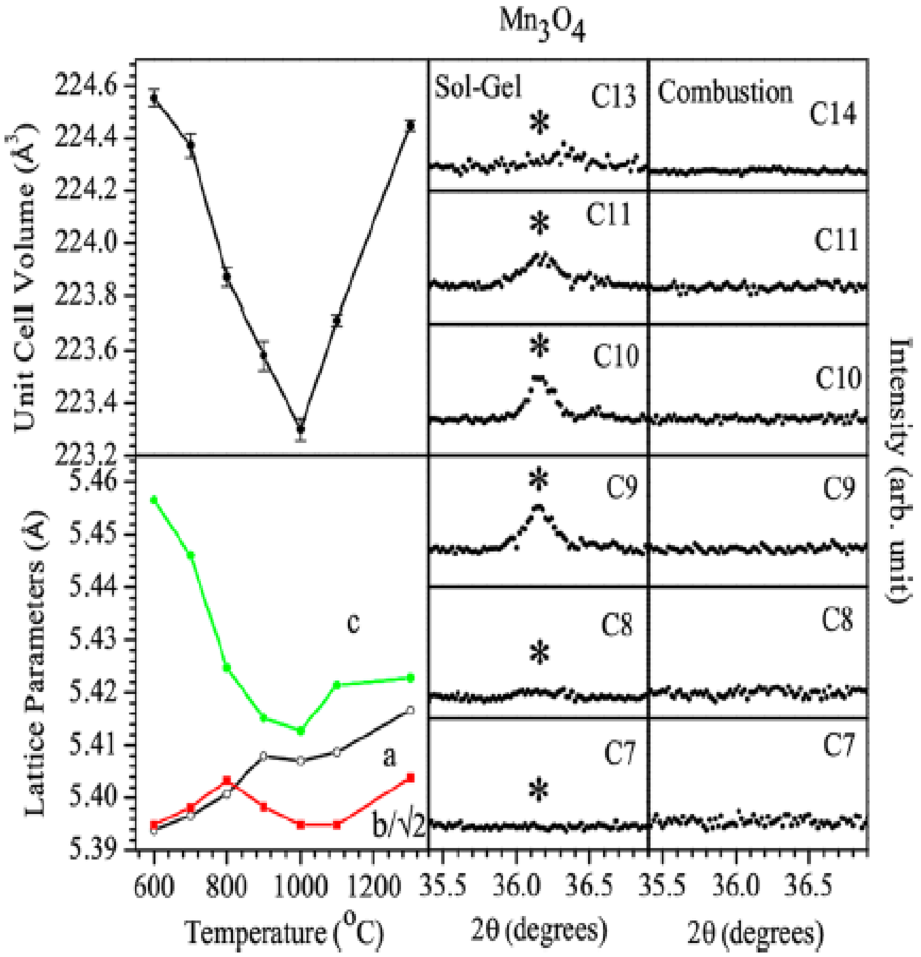

Fig. 3.15. Variation of unit cell volume (left upper panel) and lattice parameters (left lower panel) for $La_{0.5}Ca_{0.5}MnO_3$ samples prepared by sol-gel method and calcined at various temperatures. The middle panel shows the evolution of strongest peak of Mn_3O_4 impurity (around 2θ ≈36.17) for samples calcined at various temperatures. The samples calcined at 700, 800, 900, 1000, 1100 1300 °C are denoted as C7, C8, C9, C10, C11 and C13 respectively.

However, if this explanation is valid then the unit cell volume should not increase by decreasing the particle size as the hydrostatic pressure caused by excess surface energy is expected to be higher for lower crystallite size.

3.4 Origin of Suppression of Charge Ordering Transition

As discussed in the preceding sections there can be three reasons for suppression of charge ordering transition and stabilization of the ferromagnetic state in the nanocrystalline samples namely (i) enhanced e_g electron bandwidth due to increased unit cell volume (ii) non-stoichiometry when the unit cell volume is lower than the bulk and (iii) strain in the samples caused by hydrostatic pressure etc. We calculated the bandwidth for the LCMO using empirical formula $W \propto \cos\omega/d_{Mn-O}^{3.5}$, for the bulk and nano samples [Medarde et al. (1995); Arulraj et al. (1998)]. Even though this calculation is not very accurate when the bond angles and bond lengths are highly distorted but it gives some idea about the relative change. Using this relationship we find that the bandwidth for nano LCMO (C8) is ~0.0978(2) which is higher than the bulk bandwidth ~0.0965(2). Thus our observation of increased unit cell volume with decreasing particle size, increased bandwidth, increased T_C and stabilization of ferromagnetic state in nano samples is in order. A similar observation has been made by Zhang et al. (2006) in $La_{0.6}Pb_{0.4}MnO_3$ where T_C increases with bandwidth. In fact, Sarkar et al. (2008) have reported that with decreasing crystallite size the ferromagnetic to paramagnetic transition temperature (T_C) increases. This suggests that the bandwidth for the nanosize samples is increasing with decreasing crystallite size leading to enhancement in the T_C. The increased unit cell volume is expected to significantly enhance the bandwidth for e_g electrons thereby preventing the charge ordering transition. It is well known for the $La_{0.5}(Ca_{0.5-x}Sr_x)MnO_3$ ceramics that substitution of Ca^{2+} by Sr^{2+} increases the unit cell volume and the e_g electron bandwidth and leads to suppression of charge ordering transition [Sundaresan et al. (1998)]. Similarly substitution of Nd^{3+} by bigger ion La^{3+} in $Nd_{0.5}Sr_{0.5}MnO_3$ increases the e_g electron bandwidth and T_C stabilizing the ferromagnetic state down to low temperatures with the absence of charge ordering transition [Moritomo et al. (1997)]. Thus we may conclude that increased unit cell volume and e_g electron bandwidth is responsible for to suppression of charge ordering transition in nanocrystalline LCMO, NCMO and PCMO samples. Ferromagnetic phase may get stabilized either by increased bandwidth due to increased unit cell volume as observed by us or by off stoichiometry as reported for $LaMnO_3$. A careful inspection of the diffraction pattern of LCMO reported by Sarkar et al. (2008) reveals that weak reflection corresponding to the Mn_3O_4 is present in their samples [see the two theta positions ~36.17]. We analysed the strain contributions in the bulk and nanocrystalline LCMO, PCMO and NCMO samples using Rietveld method. The presence of strain in the samples leads to anisotropic broadening of the diffraction profiles and can be estimated by using the anisotropic profile shape function proposed by Stephens et al. (1999). We have summarized the results of strain analysis for the bulk and nano crystalline samples in Table IV. As can be seen in this table the nanocrystalline samples of all the three manganites have significantly larger anisotropic strain than the bulk samples. Particularly the S_{400}, S_{202} and S_{220} coefficients are very high suggesting larger strain in nano samples.

Table 4.4. Generalized S_{HKL} strain parameters of bulk and nanocrystalline LCMO, NCMO and PCMO ceramics

Anisotropic Strain parameter	S_{400}	S_{040}	S_{004}	S_{220}	S_{202}	S_{022}
LCMO14	0.24(3)	0.084(8)	0.09(2)	0.00	0.14(7)	0.00
LCMO6	3.5(7)	16(1)	3.7(5)	95(6)	42(2)	14(2)
NCMO11	2(1)	0.7(5)	0.3(8)	0.00	5(3)	0.00
NCMO7	179(3)	3(2)	13(3)	42.7(2)	168(9)	17(9)
PCMO11	2.3(1)	0.4(2)	3.44(3)	-1.6(3)	1.6(1)	3.6(2)
PCMO6	40(3)	1.8(1)	2.7(3)	48 (3)	113(6)	10(1)

It is well known that the magnetic state of rare earth manganites can get significantly altered by strain [Gutierrez et al. (2014)]. Application of hydrostatic pressure, which introduces significant strain in the sample, is also reported to significantly affect the magnetic state of rare earth manganites [Moritomo et al. (1997); Kozlenko et al. (2007); Dhiman et al. (2010)]. As given in Table IV, reduction of crystallite size to nanometer range is introducing significant strain in the samples and might have very crucial role in stabilizing ferromagnetic metallic state at lower temperatures.

3.5 Summary

To summarize, we have investigated the origin of suppression of charge ordering transition in nanocrystalline doped rare earth perovskites manganites by studying crystal structure and magnetic properties of $La_{0.5}Ca_{0.5}MnO_3$, $Nd_{0.5}Ca_{0.5}MnO_3$ and $Pr_{0.5}Ca_{0.5}MnO_3$ samples of various crystallite sizes obtained by calcining at various temperatures. The unit cell volume is enhanced in all the three manganites by crystallite size reduction in the nanocrystalline form which is attributed to the increased e_g electron bandwidth. This leads to suppression of charge ordering transition and stabilization of ferromagnetic state down to low temperatures in nanocrystalline samples. The crystal structure is orthorhombic in Pnma space group for both bulk and nanocrystalline samples but the lattice parameters and Mn-O bond lengths are significantly affected by crystallite size reduction in the nanocrystalline samples. A comparative study of Sol-Gel derived samples suggests that smaller unit cell volume of nanocrystalline samples than the bulk samples, reported by some authors, is linked with the non-stoichiometry of the samples which can also suppress the charge ordering transition and stabilize the ferromagnetic state in nanocrystalline form. The nanocrystalline samples have significant anisotropic strain which may have significant role on the magnetic and phase transition behavior of these samples. More work on thin film samples of these manganites having various form of anisotropic strain is needed to exactly ascertain the role of strain on the magnetic and phase transition behavior of these materials.